Review of photoacoustic imaging for microrobots tracking *in vivo* [Invited]

Dengfeng Li (李登峰)[†], Yachao Zhang (张雅超)[†], Chao Liu (刘 超)[†], Jiangbo Chen (陈江波), Dong Sun (孙 东)[*], and Lidai Wang (王立代)[**]

Department of Biomedical Engineering, City University of Hong Kong, Hong Kong 999077, China

[*]Corresponding author: medsun@cityu.edu.hk
[**]Corresponding author: lidawang@cityu.edu.hk

Microrobots-assisted drug delivery and surgery have been always in the spotlight and are highly anticipated to solve the challenges of cancer *in situ* treatment. These versatile small biomedical robots are expected to realize direct access to the tumor or disease site for precise treatment, which requires real-time and high-resolution *in vivo* tracking as feedback for the microrobots' actuation and control. Among current biomedical imaging methods, photoacoustic imaging (PAI) is presenting its outstanding performances in the tracking of microrobots in the human body derived from its great advantages of excellent imaging resolution and contrast in deep tissue. In this review, we summarize the PAI techniques, imaging systems, and their biomedical applications in microrobots tracking *in vitro* and *in vivo*. From a robotic tracking perspective, we also provide some insight into the future of PAI technology in clinical applications.

Keywords: photoacoustic imaging; PACT; OR-PAM; microrobots tracking; clinical applications.
DOI: 10.3788/COL202119.111701

1. Introduction

Scientists have invented microrobots that can directly reach the site of disease to perform medical tasks. Microrobots-assisted *in vivo* drug delivery, release, and *in situ* surgery are therefore seen as very promising medical solutions[1]. Microrobots, acting as the carriers, can efficiently deliver drugs for tumor treatment[2], and they can also even culture and transport cells *in vivo* for tissue engineering[3]. Over the past decades, actuation and control have been the focus of the microrobots' research[4]. Under the optical[5,6], magnetic[7,8], chemical[9,10], and biological fields[11], microrobots have already been able to achieve a variety of effective movement for *in vitro* or *in vivo* environments[12]. In recent years, more researchers are focusing on how microrobots can be truly applied for clinical therapy. Many *in vivo* experiments on small animals have also been carried out to validate and advance the *in vivo* application of the microrobots[13–16].

However, in the current stage, one of the biggest challenges in extending microrobots to the clinic is still *in vivo* tracking. Without real-time and high-resolution tracking as the feedback, it is difficult to achieve effective control and movement of microrobots in the living body. Scientists have used many biomedical imaging methods for *in vivo* tracking, such as ultrasound (US) imaging[17,18], fluorescence imaging[3], magnetic resonance imaging (MRI)[13], and X-ray tomography[19]. However, all of these methods have their limitations[20]. For example, US imaging shows a low signal-to-noise ratio and low special resolution. Fluorescence imaging is limited by the limited penetration depth in the human body. For MRI, the real-time acquisition is challenging. The low spatial resolution of X-ray imaging is also insufficient for micron-scale robot tracking. Therefore, medical microrobots still need better imaging[21].

Photoacoustic imaging (PAI) is showing outstanding advantages in the imaging of microrobots *in vivo*. PAI combines the contrast of optical absorption with the spatial resolution of US for deep imaging in tissue. The resolution of PAI ranges from several to 100 μm for imaging in the millimeter- to centimeter-depth tissue. Briefly, the greatest advantage of PAI is its ability of label-free imaging across scales, from nanometers to hundreds of microns, from microscopic to macroscopic, from cell nuclei to human organs. Different from tissue and body fluids, microrobots are often covered with metallic materials, which have strong absorption of light and produce a strong photoacoustic (PA) signal for high-contrast, high-resolution imaging, which provides a solid basis for *in vivo* PA tracking of the microrobots[22,23].

In this review, we systematically summarize the PAI principles, techniques, systems, and biomedical applications in microrobots tracking and navigation. As summarized in Fig. 1, the
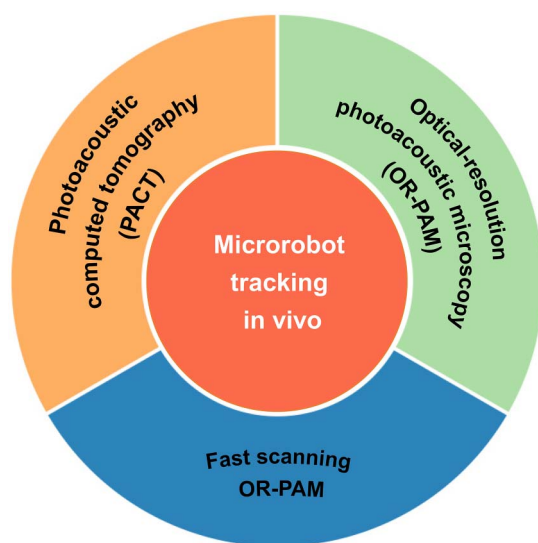
Fig. 1. Schematic summary of microrobots tracking *in vivo* based on PAI.

Fig. 2. *In vivo* PAI from organelles to organism. (a) A typical tubular-shaped mitochondrion in mouse embryonic fibroblasts[28]. (b) Capillary beds and RBCs in mouse ears[29]. (c) Heartbeat-encoded arterial network mapping of a 27-year-old healthy female volunteer's breast cross-sectional image[30]. (d) Complete maximum intensity projection (MIP) PA image of the hand[31].

PAI systems including PA computed tomography (PACT), optical-resolution PA microscopy (OR-PAM), and fast scanning OR-PAM are highlighted and demonstrated from the perspective of microrobots tracking. In the future, further system integration and upgrades will continue to be necessary to enable the real PAI clinical applications.

2. Photoacoustic Imaging

PAI is a new hybrid imaging technique arising from the PA effect, which is based on the target's intrinsic absorption property[24]. Despite that, the PA effect was first discovered by Alexander Graham Bell in 1880, and it was rapidly exploited as an imaging technology only after the coming of computers, ultrasonic transducers, and lasers[25]. The principle is that when the pulsed laser beam shines the tissue, the target will absorb the light and generate instantaneous heat. The heat will cause thermal expansion and generate mechanical ultrasonic waves as the PA wave. After collecting the PA wave by an ultrasonic transducer and reconstructing the signal, an image reflecting the light absorption distribution in biological tissue can be required[26,27]. PAI can help us listen to the sound of light and see the color of biological tissue itself.

PAI combines the advantages of pure optical and ultrasonic imaging methods, making it a unique inherently background-free detector for label-free multiscale high-resolution imaging of biological structures, ranging in size from organelles to an organism[28–32]. As shown in Fig. 2, the tubular-shaped mitochondrion (organelle), capillary beds and red blood cells (RBCs, cell), breast cross-sectional image (organ), and the hand (organism) are all clearly rendered by means of PAI, derived from its high-resolution and multifunctional tissue imaging properties. Therefore, multiscale PAI enables tracking imaging of microrobots with different sizes for different targets.
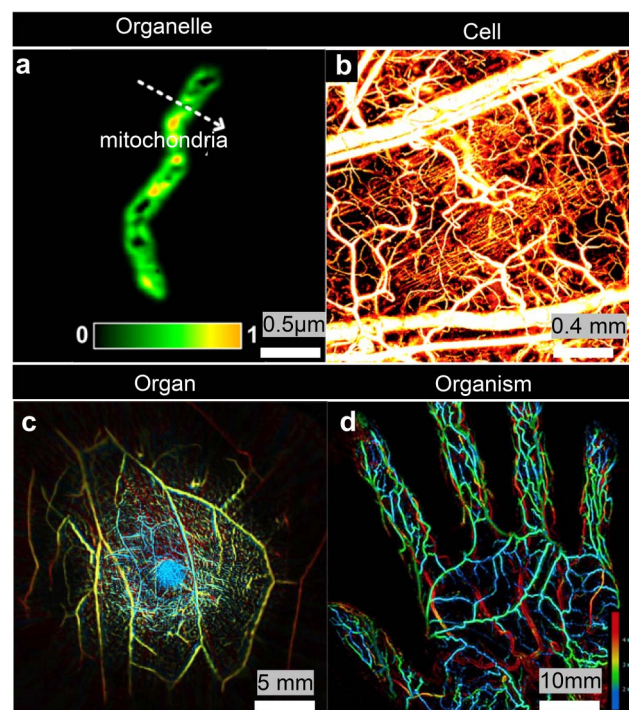
Based on a unique absorption spectrum, a different target can be classified by PAI via different wavelengths, making it a distinctive imaging technique for multi-contrast and multi-parameter sensing including the hemoglobin concentration (CHb)[2], labeled tumor cells[33], oxygen saturation (sO$_2$)[29], blood flow speeds (BF)[34], and labeled lymphatic vessels[35], as shown in Fig. 3. According to the selected wavelength ranging from ultraviolet to near-infrared, PAI can be used for endogenous contrast imaging of DNA/RNA, myoglobin, hemoglobin, lipid, etc.[35–37]. Considering injecting an exogenous agent into living animal to label molecules[38,39], PAI can also be used for exogenous contrast imaging. The PA signal from optical absorption can be used to derive many physical, chemical, and functional parameters of the absorber and the surrounding microenvironment. For instance, the PA signal measured at an isosbestic wavelength can be calibrated to determine the CHb. By using at least two wavelengths, PAI can determine the relative concentrations of oxygenated hemoglobin (HbO2) and deoxygenated hemoglobin (HbR), and thus quantify blood sO$_2$. By using PA Doppler[40,41] or the thermal clearance method[34], PAI can be used for measuring BF. By labeling with exogenous contrast agents, PAI can also be used to image neurons, lymphatic vessels, and tumor cells. Multi-parameter PAI can provide a more sophisticated understanding, making it conducive for diagnosis, staging, and treatment of diseases.
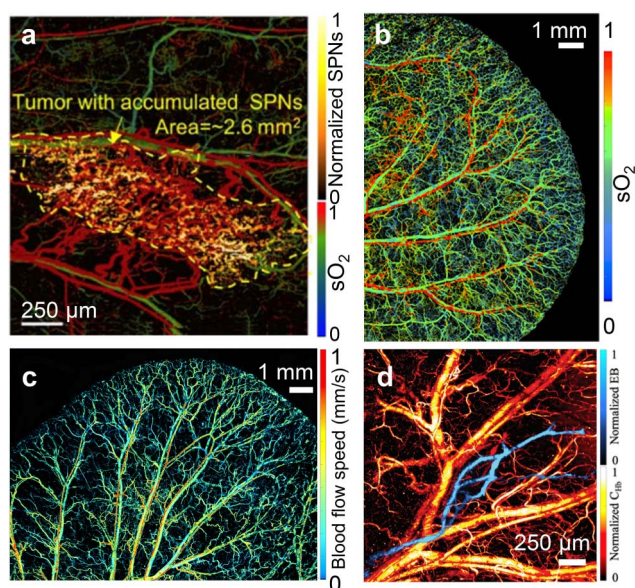
Fig. 3. Multi-contrast and multi-parameter PAI. (a) Labeled tumor and surrounding vascular vessels[33]. (b) Oxygen saturation (sO₂) in mouse ear[29]. (c) BF in mouse ears[34]. (d) Labeled lymphatic and blood vessels[35].

Based on these properties, by choosing a suitable wavelength, PAI can be used to induce the simultaneous imaging of endogenous contrast agents (blood vessels) and an exogenous contrast agent (microrobots). As shown in Fig. 4, in an *in vivo* environment, the microrobots are actuated by a variety of external fields, such as magnetic fields, and then perform therapeutic operations at the disease site. When the microrobots start to work, PAI can be used to track the microrobots and, at the same time, image and record the feedbacks of molecules (may reflect changes of functionality) *in vivo*. PAI can provide high-resolution and high-contrast multiscale information of structure, morphology, function, and metabolism for biological application, which has broad application prospects in the field of biomolecular imaging.
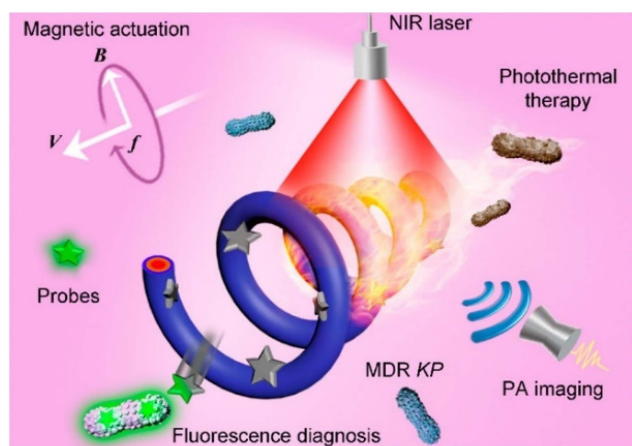

Fig. 4. PAI-trackable magnetic microswimmers. Reproduced with permission from Ref. [42].

Nowadays, the main research branches of PAI include PACT[43–45], PA microscopy (PAM)[46,47], and intravascular PAI (IVPAI)[48]. PAM can be further classified into OR-PAM[49,50] and acoustic-resolution PAM (AR-PAM)[51].

3. Photoacoustic Computed Tomography Guiding Microrobots *in vivo*

PACT is a reconstruction-based imaging method in PAI fields. Different from the configuration scheme of laser excitation and acoustic detection in PAM imaging[33], the PACT system adopts a wide-field illumination scheme to cover the tissue and collects the generated acoustic signals from spatially distributed sensors[52–54,55]. The sensors array can be arranged in different layouts in three-dimensional (3D) space to achieve a wider field of view (FOV) detection and video-rate imaging speed, such as linear array[56,57], curved array[58–60], hemispherical array[61], or planar array[62]. Because of the diffused photons excitation and array-based computing reconstruction, PACT can achieve much deeper imaging depth than PAM imaging[62].

Benefitting from the advantages of the wider FOV, video-rate imaging speed, and deeper imaging depth, PACT has demonstrated enormous potential in tumor diagnosis and therapy[63–67], drug delivery[68], and precise localization and tracking in surgical navigation[69]. In 2017, Wang's group demonstrated a stand-alone single-impulse panoramic PACT (SIP-PACT) for *in vivo* whole-body dynamics at high spatiotemporal resolution[43]. The SIP-PACT system simultaneously integrates high spatiotemporal resolution, deep penetration, multiple contrasts, full-view fidelity, and high detection sensitivity.

As shown in Fig. 5, our laboratory further tries to integrate plane-wave US imaging and single-shot PA imaging and has developed a video-rate dual-modal imaging system using a ring-array-based US transducer[60]. The system has been well demonstrated in animal whole-body dynamic imaging and human finger imaging.

Besides the above-mentioned excellent imaging performance, PACT is also spectrum sensitive and free from ionizing radiation and electromagnetic interference. Therefore, PACT can be a better choice for microrobots guidance to execute specific tasks within hard-to-reach regions *in vivo*, such as thrombus removal, drug delivery, and tumor therapy.

The first, to the best of our knowledge, reported integration platform of the microrobotic system and PACT imaging system for investigation *in vivo* is from Wang's group[70]. They designed a 512-element full-ring PACT system to guide micromotors in the gastrointestinal (GI) tract *in vivo* [Figs. 6(a) and 6(b)]. The micromotors were enveloped in the enteric protective microcapsules and can be controlled to release through near-infrared CW laser irradiation [Figs. 6(c) and 6(d)]. After release, the micromotors can use autonomous propulsion [Fig. 6(e)]. The imaging system has an excellent isotropic spatial resolution (125 μm), video-rate imaging speed (50 Hz), and larger *in vivo* penetration depth (48 mm). Therefore, the drug-loaded micromotors can be monitored in real-time during migration *in vivo* and then
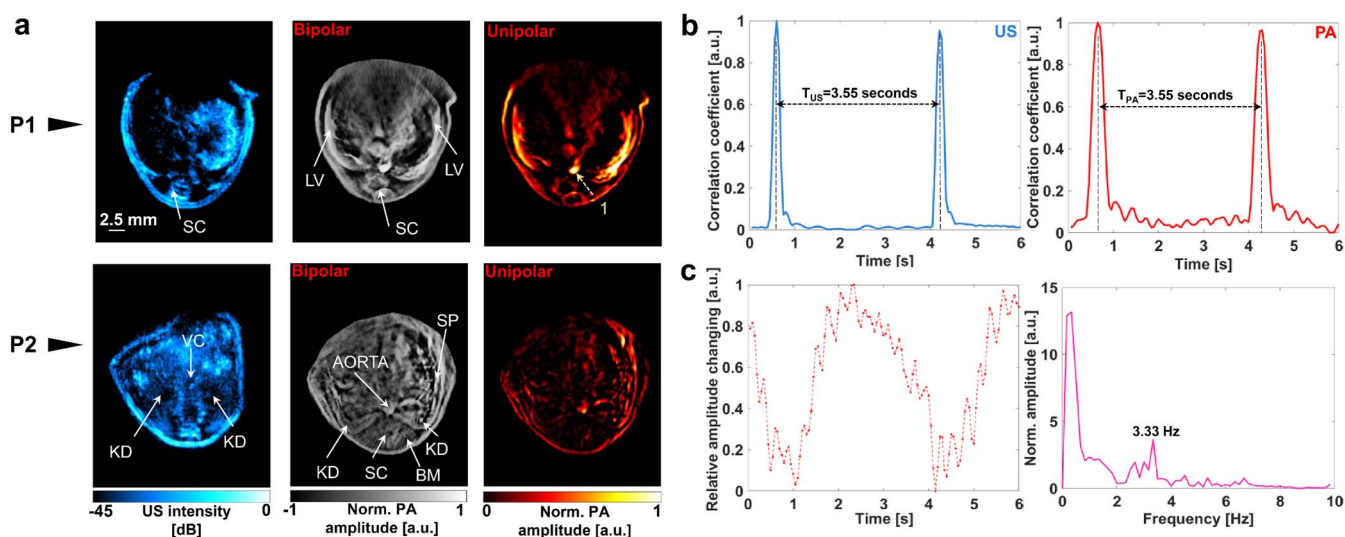
Fig. 5. *In vivo* US/PACT imaging of the liver and kidney. (a) US image, bipolar PA image, and unipolar PA image at the cross section of the liver (P1) and kidney (P2); arrow 1 denotes the tracked and recorded artery blood vessel position. (b) Respiration motion time interval estimation according to the correlation coefficient calculation. (c) PA amplitude changing as a function of time at the position marked by an arrow [P1 in (a)] and its corresponding spectral analysis. Reproduced with permission from Ref. [60].

released once they reached the targeted therapy regions. Figures 6(f)–6(i) show the result of microrobot movement in the intestines.

Precise delivery of therapeutic cells loaded by the microrobots to the targeted tumor region through the vascular region is promising in precision medicine. This therapy method can respond to cancer dynamically with few side effects and will not cause excessive immune response[71]. Based on this conception, our laboratory integrates gradient magnetic field and PACT/US dual-modal imaging into a platform to actuate and monitor the cell-loaded microrobots (Fig. 7). This work demonstrated the feasibility of precise delivery of therapeutic cells in vascular and its therapeutic effect using the microrobots *in vivo* for the first time, to the best of our knowledge[23]. The microrobots with a burr-like porous spherical structure are mainly made of polyethylene glycol diacrylate (PEGDA) and pentaerythritol triacrylate (PETA). The structure features enhance the magnetic driving and cell-carrying ability, while the material composition ensures the degradability and mechanical performance. We also systematically investigated the effect of the number of microrobots and the tissue depth on the PA signal amplitude. Finally, the *in vitro* imaging depth can achieve 20 mm. Benefitting from the advantages of dual-modal imaging, the system can real-time navigate the cell-loaded microrobots through the inferior vena cava of nude mice at a depth of 6 mm.

Because of the remarkable imaging performance and compatibility features, PACT imaging is attracting more and more attention in the areas of microrobot characterization, drug delivery, and tumor therapy since 2019[42–73]. Some problems faced by PACT imaging, such as limit of view when adopting a linear-array US transducer and depth- or wavelength-dependent fluence compensation, are being alleviated using some new

technologies[74]. Different imaging modalities, such as US imaging and optical imaging (fluorescence imaging, optical coherence tomography, etc.), can be integrated into PACT imaging to provide complementary information. All of these will further enhance the superiority in microrobots imaging-guiding fields.

4. High-Resolution Tracking by Optical-Resolution Photoacoustic Microscopy

With the PACT system, the images of the microrobots or swarm are often bright spots. Its isotropic spatial resolution of over 100 μm is not enough to see the clear shape of the microrobots around the 100 μm size. As a result, the movement of the microrobots tracked by the PACT system is shown as a few moving bright spots. Therefore, high-resolution PAI is still required to observe the shape and position of a single microrobot, especially for those with sizes less than 100 μm.

Compared with other biomedical imaging technologies that can only look at the microrobots' trajectory, distribution, and features gathered on the tissue in a macroscopic view, OR-PAM can realize both subcellular multifunctional and robotic imaging, providing a microscopic view of microrobotic research.

Last year, our laboratory demonstrated the PAI of a single microrobot in blood, as shown in Fig. 7. The OR-PAM system in Fig. 8(a) shows that the optical excitation and ultrasonic detection in OR-PAM are aligned confocally, enabling it a micron-scale lateral resolution, which enables sub-cellular-scale features to be resolved.

The main task for the microrobots is to reach the disease site within the organs. The blood vessel is the best channel for this,
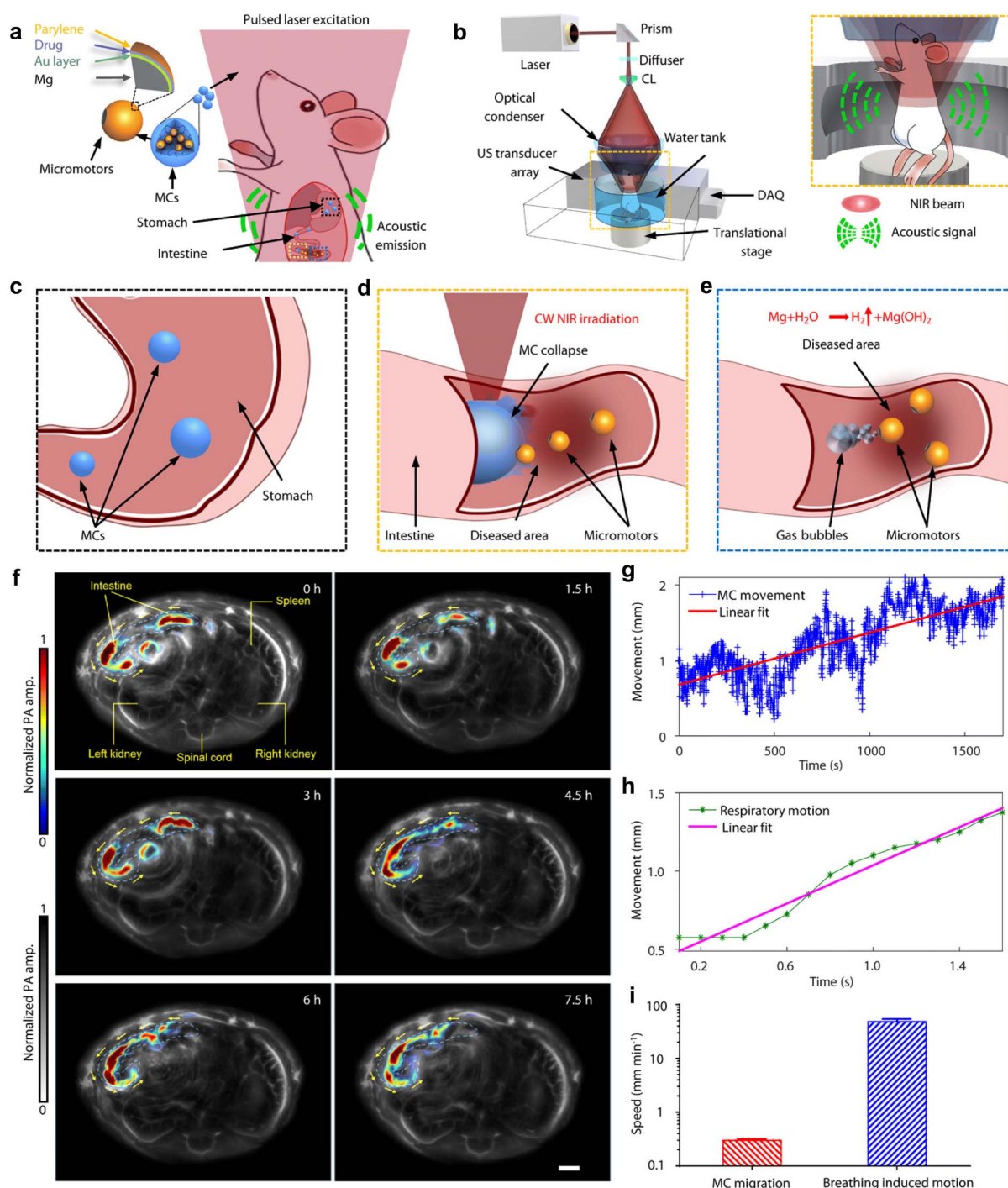
Fig. 6. Microrobotic system guided by PACT *in vivo*. (a) Microrobots in the mouse with PA excitation and generation. (b) PACT imaging setup. (c) Enteric coating protection in the stomach. (d) CW NIR laser irradiation for micromotor release in the intestine. (e) Microrobots propulsion to the therapy region. (f) Dynamics evaluation of PACT-guided microrobots movement in the intestine. (g) Movement displacement caused by the microrobots migration. (h) Movement displacement caused by respiration. (i) Speed comparison of microrobots migration and the respiration-induced movement. Reproduced with permission from Ref. [70].

as the blood is circulated throughout the body. Therefore, precise tracking of a microrobot in the bloodstream is quite essential. As demonstrated in Fig. 8(b), the ~50 μm micro-rocket robot is successfully tracked at a 3.2 μm resolution with the OR-PAM system in blood. When the micro-rocket moved in the blood vessel model, the OR-PAM acquired multiple images

at different positions with clear information of the structure and depth of the single micro-rocket.

For the current system in Fig. 8(a), the real-time tracking of microrobots remains difficult to achieve due to its slow imaging speed. In vessels with high flows, only real-time tracking enables effective control for the microrobots. Therefore, developing the
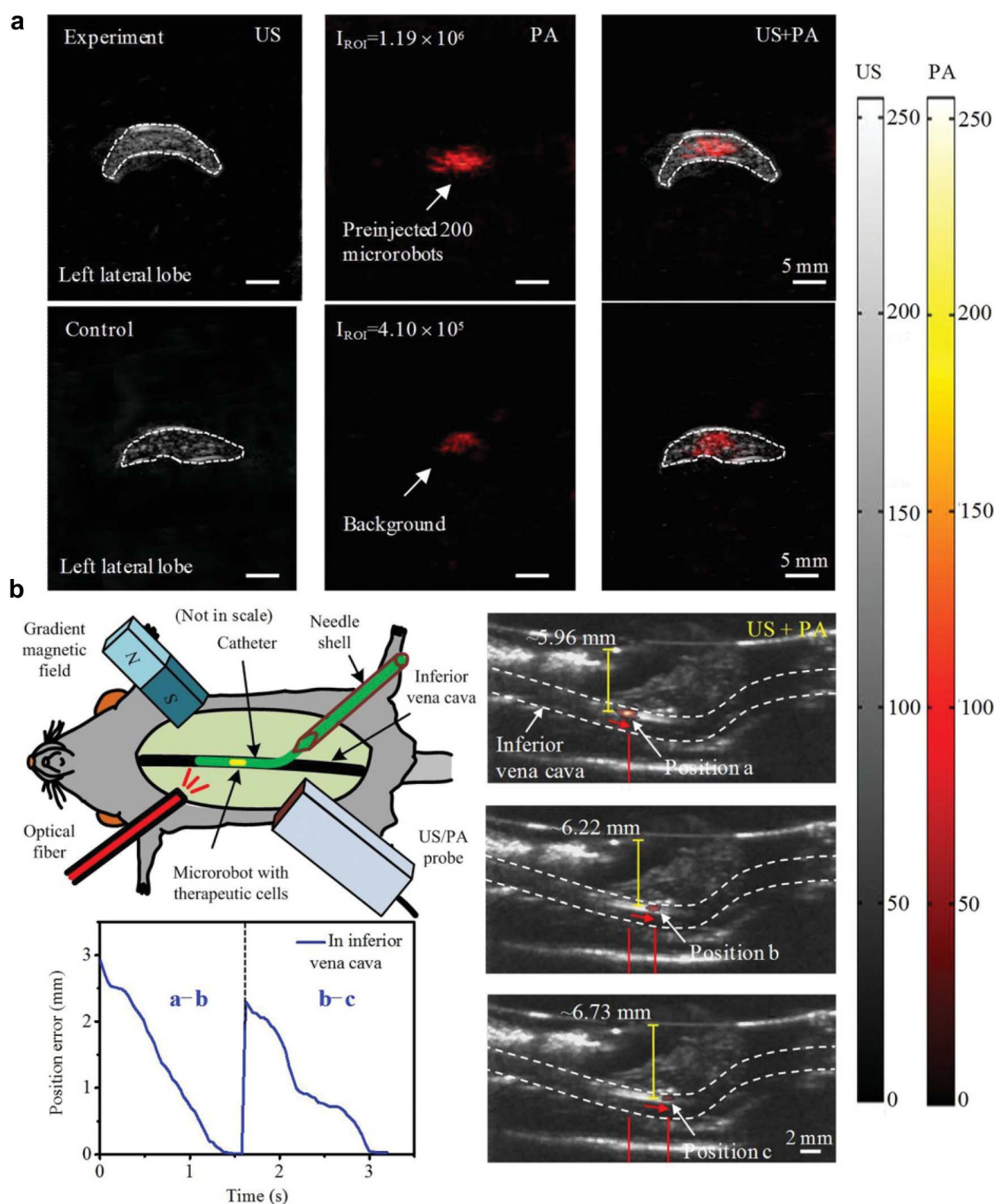
Fig. 7. Microrobots imaging and navigation using developed PACT/US dual-modal system. (a) Comparison of PA signal amplitude in the left lateral lobe with and without injection microrobots clusters. The microrobots were injected through the portal vein, and the PA images were overlayed on the US images. (b) PA/US imaging guiding microrobots in the inferior vena cava of the mouse. Reproduced with permission from Ref. [23].

faster OR-PAM system will be significant to advance high-resolution PA tracking *in vivo*.

5. Fast Scanning OR-PAM

A single microrobot can be tracked with high resolution by employing OR-PAM. To track the moving microrobots in the vessel, we need to use a fast scanning OR-PAM with a high C-scan rate over a large FOV.

There are mainly three approaches that have been proposed to achieve a high imaging speed. Firstly, due to object inertia, a fiber-based OR-PAM system has a higher scanning speed compared to a fixed free-space OR-PAM system, because the PA probe has a smaller mass than the sample platform and easily achieves fast translation[75–77]. Secondly, a single-shot laser
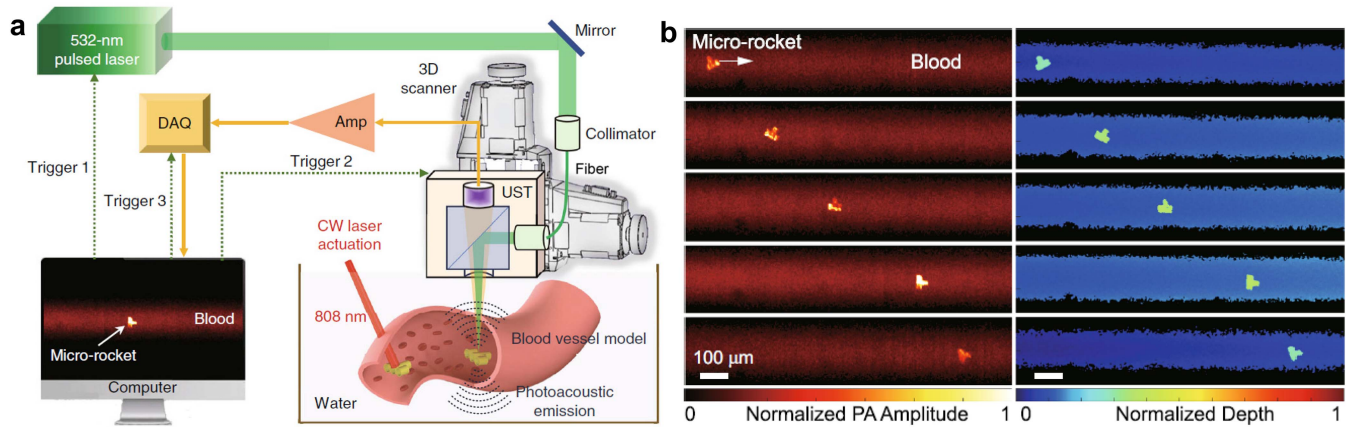
Fig. 8. PAI of a single microrobot in blood. (a) Optical resolution PA system. (b) High-resolution PA tracking of a single micro-rocket in the blood vessel model. Reproduced with permission from Ref. [22].

source is indispensable for offering the fast short-pulse laser with enough energy[49]. Furthermore, a fast scanner with a large FOV is a significantly important part that achieves fast scanning. Traditional OR-APM often uses the stepper motor to translate the PA probe. The fast axis is limited to around 2 Hz over the 5 mm range[33]. Some new scanners have been developed to improve the imaging speed.

The galvanometer can effectively improve the scanning speed, while it cannot work in water and has a serious contradiction between FOV and sensitivity[63,78–80]. A water-immersible microelectromechanical system (MEMS) scanner has been developed as the fast axis of OR-PAM. It is easy to achieve fast vibration with a lightweight mirror. It has several hundred or even thousands of B-scan rates. The designed B-scan ranges from tens of micrometers to several millimeters[46,50,81]. A drawback of the water-immersible MEMS scanner is that it becomes vulnerable if working for a long time, resulting in distorted images. A water-immersible galvanometer is proposed to achieve stable scanning in water and keep large FOV[50,82], offering an alternative to enhance the scanning speed of OR-PAM.

The water-immersible MEMS scanner and water-immersible galvanometer occupy the workspace, resulting in a smaller acoustic lens numerical aperture (NA). The voice-coil scanner is a high-speed motion platform that can achieve fast scanning without sacrificing sensitivity. It has been successfully used as the fast axis of OR-PAM, as shown in Fig. 9(a)[83,84]. The PA probe is mounted on the voice-coil platform. The B-scan rate of the voice-coil scanner improves by tens of times compared to that of the stepper motor over a millimeter scale. The voice-coil scanner enables the OR-PAM to track the flowing single cell of the mouse brain and monitor the sO_2 change induced by visual stimulation in real-time, as shown in Figs. 9(b)–9(d).

To further improve the scanning speed and FOV, our laboratory developed a polygon scanner OR-PAM, as demonstrated in Fig. 10[85]. It achieved multi-wavelength imaging at a 1 MHz A-line rate. The B-line rate reaches ~500 Hz over 12 mm. Figure 10(a) shows the schematic of the polygon scanner
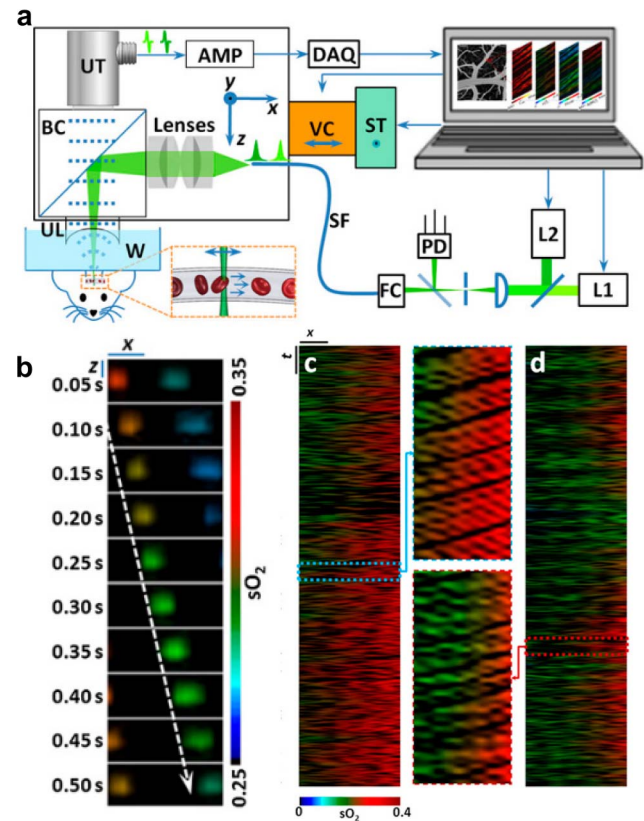

Fig. 9. Voice-coil-driven fast-scanning OR-PAM. (a) Schematic of the system. (b) Snapshots of single RBCs releasing oxygen in a mouse brain. (c) sO_2 images without continuous visual stimulation. (d) sO_2 images with 1 Hz continuous optical flashing stimulations on the left mouse eye. Reproduced with permission from Ref. [83].

OR-PAM. A laser source based on the stimulated Raman scattering (SRS) effect is used to generate 532 nm and 558 nm laser beams. The laser beam is aligned to the acoustic beam, thus maximizing the sensitivity. The polygon scanner scans the laser

beams and acoustic beams over the 12 mm range. Figure 10(b) shows an sO₂ image of the whole mouse ear. As shown in Fig. 10(c), it can track the flowing iron particle. It offers a potential fast imaging tool with a large FOV for microrobots tracking.
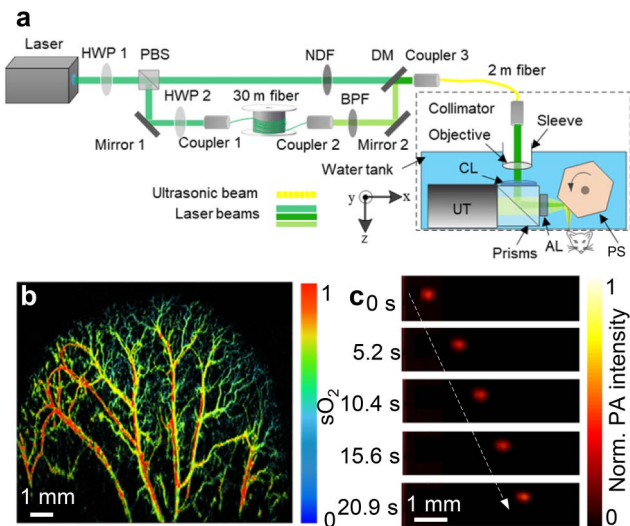

Fig. 10. Polygon-scanning fast OR-PAM. (a) Schematic of the system. (b) sO₂ image of the mouse ear; C-scan time is ∼5 s. (c) Flowing iron particle tracking. Reproduced with permission from Ref. [85].

Table 1. Scanning Speed and Range of Fast-Scanning PAM Systems.

Methods	B-scan Rate (Hz)	B-scan Range (mm)
Galvanometer[79]	1800/100	0.1/6
Water-immersible galvanometer[50,86]	500	>2.4
Voice-coil[84]	40	∼5
Single-axis water-immersible MEMS[46]	400	>3
Dual-axis water-immersible MEMS[87]	5	9
Polygon mirror[85,88]	∼500	∼12

Finally, we summarized some typical fast scanning OR-PAMs' imaging speed and scanning range in Table 1, offering alternative methods for high-resolution tracking of microrobots *in vivo*.

The water-immersible galvanometer, water-immersible MEMS scanner, and polygon scanner have higher scanning speeds compared with other reported scanners. It is possible for them to achieve real-time tracking of microrobots. Among them, polygon-scanning fast OR-PAM shows outstanding advantages in the FOV. For example, with the same B-scan rate of 500 Hz, the B-scan range of the water-immersible galvanometer and MEMS scanner only reaches ∼4 mm, while the polygon mirror scanner reaches as high as 12 mm. To achieve a 12 mm × 12 mm FOV, the water-immersible galvanometer and MEMS-scanning OR-PAM have to adopt an imaging stitching method due to the limited B-scan range, three times that of polygon-scanning OR-PAM to achieve the same FOV. Therefore, the polygon scanner is a potential tool for broadening the application of OR-PAM in microrobots tracking.

Overall, this review details the biomedical applications of PAI for microrobots tracking in terms of the different PAI systems and techniques. To compare these imaging systems more clearly and to identify their range of applications, Table 2 is presented to summarize the three types of highlighted PAI systems, including SIP-PACT, OR-PAM, and polygon-scanning fast OR-PAM. For PACT, its advantages are the large imaging penetration depth and the real-time imaging capability, which can be used for whole-body dynamics and function imaging for small animals. Therefore, for real-time microrobots tracking in the deep tissue of the living body, PACT would be the best option. However, the limited resolution makes it difficult to track an individual microrobot less than 100 μm. At this point, the OR-PAM compensates well for this deficiency, as its resolution can reach below 10 μm. For the high-resolution microrobots tracking in epidermal blood vessels or tissue, OR-PAM could be used as a priority. Moreover, the polygon-scanning fast OR-PAM also demonstrates fast imaging capabilities, providing an excellent option for high-resolution real-time imaging for microrobots tracking.

Currently, all microrobots tracking using PAI is limited to *in vitro* or small animal bodies. More time is needed for the real application of microrobots tracking to the human body.

Table 2. Summary of PAI Systems in the Review for Microrobots Tracking.

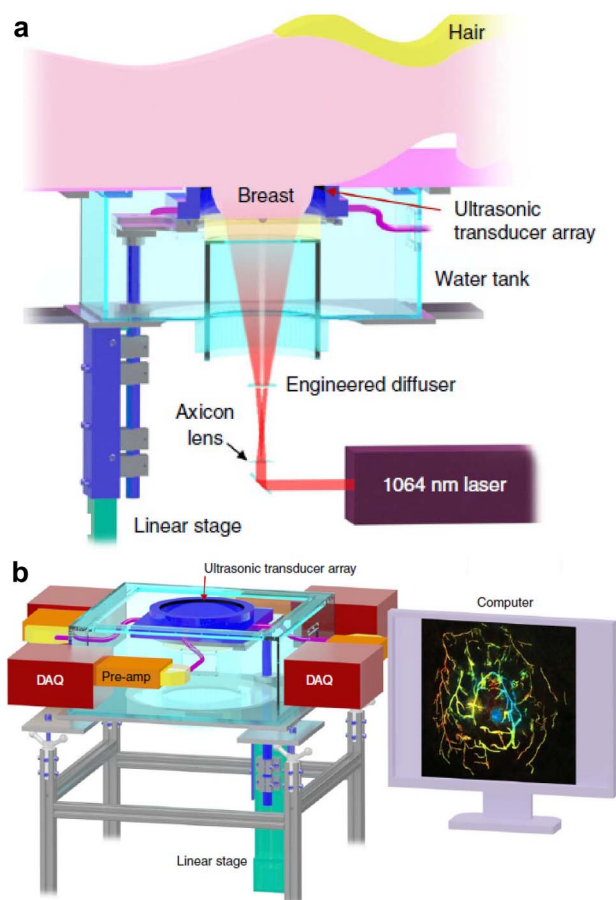| PAI System & Techniques	Resolution	Imaging Depth	Advantages	Applications
SIP-PACT[43,70]	125 μm	48 mm	Whole-body dynamics and function imaging for small animals	Real-time tracking of microrobots *in vivo*
OR-PAM[22]	3.2 μm	1 mm	High-resolution imaging	High-resolution microrobots tracking in epidermal blood vessels or tissue
Polygon-scanning fast OR-PAM[85]	∼6.3 μm	0.97 mm	Fast and high-resolution imaging	Real-time and high-resolution microrobots tracking in the epidermis

Fig. 11. Single-breath-hold PACT system for breast cancer diagnosis and screening. (a) Perspective cut-away view of patient bed and optical components of the system. (b) Data acquisition components of the system. Four sets of 128-channel data acquisition systems were mapping a custom-built 512-element ring-array transducer. Reproduced with permission from Ref. [30].

PA technology for whole-body imaging of the human body is not yet mature enough, given its limited penetration depth. Therefore, PAI techniques and systems need breakthroughs first. Then, the integration of the microrobots control equipment and imaging systems will be the next step towards *in vivo* clinical application of microrobots.

6. Perspectives on Future Clinical Applications

At the current stage, PAI has not been applied to clinical tests and imaging. In contrast, US, X-ray, and MRI imaging techniques have all developed into sophisticated equipment and are used in major hospitals. Despite many current technical challenges, experts in the field of PAI have never stopped pursuing the commercialization of PAI technology. For example, in 2018, Wang's group designed the single-breath-hold PACT system for breast cancer diagnosis, as shown in Fig. 11[30]. The system featured deep penetration (40 mm), finer spatial resolution (255 μm), high 3D imaging speed (15 s), and required neither radiation nor an exogenous contrast agent. Compared with

modern mammography or contrast-enhanced MRI, PACT imaging is very competitive for future clinical applications.

To further promote clinical applications of PACT imaging, the following areas could be highlighted for research: developing new image reconstruction algorithms to improve the quality of images; integrating with different imaging modalities, such as US imaging, fluorescence imaging, and optical coherence tomography, to provide complementary information; developing new scanning systems for large area real-time imaging; and introducing novel PA excitation modes and systems to improve imaging resolution.

For the OR-PAM system, high resolution is an inherent advantage in superficial tissue imaging. However, its disadvantages of non-real-time imaging cannot be ignored. Therefore, fast OR-PAM imaging would be of great interest for clinical applications. In addition, increasing the imaging depth of the OR-PAM system is necessary and extremely challenging.

For *in vivo* tracking, microrobots within deep tissues such as human organs would be better suited to a PACT system guided robotic navigation for *in situ* drug transport and therapy. For microrobots in subcutaneous vessels or tissues, OR-PAM would be the superior choice, due to the improved high resolution. For the time being, the most efficient way of driving robots in the living body is magnetic actuation. The integration of a robotic magnetic actuation system with the PAI system will take the future of robotic clinical applications to new heights.

In conclusion, PAI provides a comprehensive and superior biomedical imaging modality for microrobots navigation in living bodies. Future advances in PAI technology and the use of PAI in clinical applications will greatly facilitate the realization of robot-assisted medicine.

References

1. J. Li, B. E.-F. de Ávila, W. Gao, L. Zhang, and J. Wang, "Micro/nanorobots for biomedicine: delivery, surgery, sensing, and detoxification," Sci. Robot. **2**, eaam6431 (2017).
2. B. E.-F. de Ávila, P. Angsantikul, J. Li, M. Angel Lopez-Ramirez, D. E. Ramírez-Herrera, S. Thamphiwatana, C. Chen, J. Delezuk, R. Samakapiruk, V. Ramez, L. Zhang, and J. Wang, "Micromotor-enabled active drug delivery for *in vivo* treatment of stomach infection," Nat. Commun. **8**, 272 (2017).
3. J. Li, X. Li, T. Luo, R. Wang, C. Liu, S. Chen, D. Li, J. Yue, S. H. Cheng, and D. Sun, "Development of a magnetic microrobot for carrying and delivering targeted cells," Sci. Robot. **3**, eaat8829 (2018).
4. X. Z. Chen, B. Jang, D. Ahmed, C. Hu, C. De Marco, M. Hoop, F. Mushtaq, B. J. Nelson, and S. Pané, "Small-scale machines driven by external power sources," Adv. Mater. **30**, 1705061 (2018).

5. Y. Wu, T. Si, J. Shao, Z. Wu, and Q. He, "Near-infrared light-driven Janus capsule motors: fabrication, propulsion, and simulation," Nano Res. **9**, 3747 (2016).

6. H. Zeng, P. Wasylczyk, C. Parmeggiani, D. Martella, M. Burresi, and D. S. Wiersma, "Light-fueled microscopic walkers," Adv. Mater. **27**, 3883 (2015).

7. S. Tottori, L. Zhang, F. Qiu, K. K. Krawczyk, A. Franco-Obregón, and B. J. Nelson, "Magnetic helical micromachines: fabrication, controlled swimming, and cargo transport," Adv. Mater. **24**, 811 (2012).

8. C. Peters, M. Hoop, S. Pané, B. J. Nelson, and C. Hierold, "Degradable magnetic composites for minimally invasive interventions: device fabrication, targeted drug delivery, and cytotoxicity tests," Adv. Mater. **28**, 533 (2016).

9. W. Gao, R. Dong, S. Thamphiwatana, J. Li, W. Gao, L. Zhang, and J. Wang, "Artificial micromotors in the mouse's stomach: a step toward *in vivo* use of synthetic motors," ACS Nano. **9**, 117 (2015).

10. D. Li, Y. Liu, Y. Yang, and Y. Shen, "A fast and powerful swimming microrobot with a serrated tail enhanced propulsion interface," Nanoscale **10**, 19673 (2018).

11. V. Magdanz, S. Sanchez, and O. G. Schmidt, "Development of a sperm-flagella driven micro-bio-robot," Adv. Mater. **25**, 6581 (2013).

12. B. Esteban-Fernández de Ávila, P. Angsantikul, J. Li, W. Gao, L. Zhang, and J. Wang, "Micromotors go *in vivo*: from test tubes to live animals," Adv. Funct. Mater. **28**, 1705640 (2018).

13. X. Yan, Q. Zhou, M. Vincent, Y. Deng, J. Yu, J. Xu, T. Xu, T. Tang, L. Bian, Y. X. J. Wang, K. Kostarelos, and L. Zhang, "Multifunctional biohybrid magnetite microrobots for imaging-guided therapy," Sci. Robot. **2**, eaaq1155 (2017).

14. B. Wang, K. F. Chan, K. Yuan, Q. Wang, X. Xia, L. Yang, H. Ko, Y. J. Wang, J. Jao, Y. Sung, P. Wai, Y. Chiu, and L. Zhang, "Endoscopy-assisted magnetic navigation of biohybrid soft microrobots with rapid endoluminal delivery and imaging," Sci. Robot. **6**, eabd2813 (2021).

15. Q. Wang, K. F. Chan, K. Schweizer, X. Du, D. Jin, S. C. H. Yu, B. J. Nelson, and L. Zhang, "Ultrasound Doppler-guided real-time navigation of a magnetic microswarm for active endovascular delivery," Sci. Adv. **7**, eabe5914 (2021).

16. Q. Wang and L. Zhang, "External power-driven microrobotic swarm: from fundamental understanding to imaging-guided delivery," ACS Nano. **15**, 149 (2021).

17. Q. Wang and L. Zhang, "Ultrasound imaging and tracking of micro/nanorobots: from individual to collectives," IEEE Open J. Nanotechnol. **1**, 6 (2020).

18. Q. Wang, L. Yang, J. Yu, P. W. Y. Chiu, Y. P. Zheng, and L. Zhang, "Real-time magnetic navigation of a rotating colloidal microswarm under ultrasound guidance," IEEE Trans. Biomed. Eng. **67**, 3403 (2020).

19. S. Jeong, H. Choi, C. Lee, G. Go, D. S. Sim, K. S. Lim, M. H. Jeong, S. Y. Ko, J. Park, and S. Park, "Therapeutic intravascular microrobot through compensation of resistance and mutual inductance in electromagnetic actuation system," Int. J. Control. Autom. Syst. **13**, 1465 (2015).

20. S. Pané, J. Puigmartí-Luis, C. Bergeles, X.-Z. Chen, E. Pellicer, J. Sort, V. Počepcová, A. Ferreira, and B. J. Nelson, "Imaging technologies for biomedical micro- and nanoswimmers," Adv. Mater. Technol. **4**, 1800575 (2019).

21. M. Medina-Sánchez and O. G. Schmidt, "Medical microbots need better imaging and control," Nature **545**, 406 (2017).

22. D. Li, C. Liu, Y. Yang, L. Wang, and Y. Shen, "Micro-rocket robot with all-optic actuating and tracking in blood," Light Sci. Appl. **9**, 84 (2020).

23. T. Wei, J. Liu, D. Li, S. Chen, Y. Zhang, J. Li, L. Fan, Z. Guan, C. Lo, L. Wang, K. Man, and D. Sun, "Development of magnet-driven and image-guided degradable microrobots for the precise delivery of engineered stem cells for cancer therapy," Small **16**, 1906908 (2020).

24. L. V. Wang and J. Yao, "A practical guide to photoacoustic tomography in the life sciences," Nat. Methods **13**, 627 (2016).

25. S. Manohar and D. Razansky, "Photoacoustics: a historical review," Adv. Opt. Photon. **8**, 586 (2016).

26. M. Xu and L. V. Wang, "Photoacoustic imaging in biomedicine," Rev. Sci. Instrum. **77**, 041101 (2006).

27. T. Feng, Y. Zhu, Y. Xie, D. Ta, J. Yuan, and Q. Cheng, "Feasibility study for bone health assessment based on photoacoustic imaging method," Chin. Opt. Lett. **18**, 121704 (2020).

28. A. Danielli, K. I. Maslov, A. Garcia-Uribe, A. M. Winkler, C. Li, L. Wang, Y. Chen, G. W. Dorn, and L. V. Wang, "Label-free photoacoustic nanoscopy," J. Biomed. Opt. **19**, 086006 (2014).

29. C. Liu, Y. Liang, and L. Wang, "Optical-resolution photoacoustic microscopy of oxygen saturation with nonlinear compensation," Biomed. Opt. Express **10**, 3061 (2019).

30. L. Lin, P. Hu, J. Shi, C. M. Appleton, K. Maslov, L. Li, R. Zhang, and L. V. Wang, "Single-breath-hold photoacoustic computed tomography of the breast," Nat. Commun. **9**, 2352 (2018).

31. Y. Matsumoto, Y. Asao, A. Yoshikawa, H. Sekiguchi, M. Takada, M. Furu, S. Saito, M. Kataoka, H. Abe, T. Yagi, K. Togashi, and M. Toi, "Label-free photoacoustic imaging of human palmar vessels: a structural morphological analysis," Sci. Rep. **8**, 786 (2018).

32. A. P. Jathoul, J. Laufer, O. Ogunlade, B. Treeby, B. Cox, E. Zhang, P. Johnson, A. R. Pizzey, B. Philip, T. Marafioti, M. F. Lythgoe, R. B. Pedley, M. A. Pule, and P. Beard, "Deep *in vivo* photoacoustic imaging of mammalian tissues using a tyrosinase-based genetic reporter," Nat. Photon. **9**, 239 (2015).

33. J. Chen, Y. Zhang, X. Li, J. Zhu, D. Li, S. Li, C.-S. Lee, and L. Wang, "Confocal visible/NIR photoacoustic microscopy of tumors with structural, functional, and nanoprobe contrasts," Photon. Res. **8**, 1875 (2020).

34. C. Liu, Y. Liang, and L. Wang, "Single-shot photoacoustic microscopy of hemoglobin concentration, oxygen saturation, and blood flow in sub-microseconds," Photoacoustics **17**, 100156 (2020).

35. C. Liu, J. Chen, Y. Zhang, J. Zhu, and L. Wang, "Five-wavelength optical-resolution photoacoustic microscopy of blood and lymphatic vessels," Adv. Photon. **3**, 016002 (2021).

36. L. Lin, J. Yao, L. Li, and L. V. Wang, "*In vivo* photoacoustic tomography of myoglobin oxygen saturation," J. Biomed. Opt. **21**, 061002 (2015).

37. B. Wang, J. L. Su, J. Amirian, S. H. Litovsky, R. Smalling, and S. Emelianov, "Detection of lipid in atherosclerotic vessels using ultrasound-guided spectroscopic intravascular photoacoustic imaging," Opt. Express **18**, 4889 (2010).

38. C. Yin, G. Wen, C. Liu, B. Yang, S. Lin, J. Huang, P. Zhao, S. H. D. Wong, K. Zhang, X. Chen, G. Li, X. Jiang, J. Huang, K. Pu, L. Wang, and L. Bian, "Organic semiconducting polymer nanoparticles for photoacoustic labeling and tracking of stem cells in the second near-infrared window," ACS Nano. **12**, 12201 (2018).

39. Y. Dai, X. Yu, J. Wei, F. Zeng, Y. Li, X. Yang, Q. Luo, and Z. Zhang, "Metastatic status of sentinel lymph nodes in breast cancer determined with photoacoustic microscopy via dual-targeting nanoparticles," Light Sci. Appl. **9**, 164 (2020).

40. H. Fang, K. Maslov, and L. V. Wang, "Photoacoustic Doppler effect from flowing small light-absorbing particles," Phys. Rev. Lett. **99**, 184501 (2007).

41. J. Yao, K. I. Maslov, Y. Shi, L. A. Taber, and L. V. Wang, "*In vivo* photoacoustic imaging of transverse blood flow by using Doppler broadening of bandwidth," Opt. Lett. **35**, 1419 (2010).

42. L. Xie, X. Pang, X. Yan, Q. Dai, H. Lin, J. Ye, Y. Cheng, Q. Zhao, X. Ma, X. Zhang, G. Liu, and X. Chen, "Photoacoustic imaging-trackable magnetic microswimmers for pathogenic bacterial infection treatment," ACS Nano. **14**, 2880 (2020).

43. L. Li, L. Zhu, C. Ma, L. Lin, J. Yao, L. Wang, K. Maslov, R. Zhang, W. Chen, J. Shi, and L. V. Wang, "Single-impulse panoramic photoacoustic computed tomography of small-animal whole-body dynamics at high spatiotemporal resolution," Nat. Biomed. Eng. **1**, 0071 (2017).

44. P. Zhang, L. Li, L. Lin, J. Shi, and L. V. Wang, "*In vivo* superresolution photoacoustic computed tomography by localization of single dyed droplets," Light Sci. Appl. **8**, 36 (2019).

45. W. Choi and C. Kim, "Toward *in vivo* translation of super-resolution localization photoacoustic computed tomography using liquid-state dyed droplets," Light Sci. Appl. **8**, 57 (2019).

46. J. Yao, L. Wang, J. M. Yang, K. I. Maslov, T. T. W. Wong, L. Li, C. H. Huang, J. Zou, and L. V. Wang, "High-speed label-free functional photoacoustic microscopy of mouse brain in action," Nat. Methods **12**, 407 (2015).

47. Y. Li, T. T. W. Wong, J. Shi, H. C. Hsu, and L. V. Wang, "Multifocal photoacoustic microscopy using a single-element ultrasonic transducer through an ergodic relay," Light Sci. Appl. **9**, 135 (2020).

48. M. Chen, H. J. Knox, Y. Tang, W. Liu, L. Nie, J. Chan, and J. Yao, "Simultaneous photoacoustic imaging of intravascular and tissue oxygenation," Opt. Lett. **44**, 3773 (2019).

49. Y. Liang, L. Jin, B.-O. Guan, and L. Wang, "2 MHz multi-wavelength pulsed laser for functional photoacoustic microscopy," Opt. Lett. **42**, 1452 (2017).

50. J. Kim, J. Y. Kim, S. Jeon, J. W. Baik, S. H. Cho, and C. Kim, "Super-resolution localization photoacoustic microscopy using intrinsic red blood cells as contrast absorbers," Light Sci. Appl. **8**, 103 (2019).

51. E. Vienneau, W. Liu, and J. Yao, "Dual-view acoustic-resolution photoacoustic microscopy with enhanced resolution isotropy," Opt. Lett. **43**, 4413 (2018).

52. P. K. Upputuri and M. Pramanik, "Recent advances toward preclinical and clinical translation of photoacoustic tomography: a review," J. Biomed. Opt. **22**, 041006 (2016).

53. L. V. Wang and S. Hu, "Photoacoustic tomography: *in vivo* imaging from organelles to organs," Science **335**, 1458 (2012).

54. J. Yao, A. A. Kaberniuk, L. Li, D. M. Shcherbakova, R. Zhang, L. Wang, G. Li, V. V. Verkhusha, and L. V. Wang, "Multiscale photoacoustic tomography using reversibly switchable bacterial phytochrome as a near-infrared photochromic probe," Nat. Methods **13**, 67 (2015).

55. X. Wang and S. Yang, "Imaging of human wrist joint by a flexible-transducer-based morphological-adaptive photoacoustic tomography: a feasibility study," Chin. Opt. Lett. **17**, 091701 (2019).

56. G. Li, L. Li, L. Zhu, J. Xia, and L. V. Wang, "Multiview Hilbert transformation for full-view photoacoustic computed tomography using a linear array," J. Biomed. Opt. **20**, 066010 (2015).

57. L. Wang, G. Li, J. Xia, and L. V. Wang, "Ultrasonic-heating-encoded photoacoustic tomography with virtually augmented detection view," Optica **2**, 307 (2015).

58. L. Lin, P. Hu, X. Tong, S. Na, R. Cao, X. Yuan, D. C. Garrett, J. Shi, K. Maslov, and L. V. Wang, "High-speed three-dimensional photoacoustic computed tomography for preclinical research and clinical translation," Nat. Commun. **12**, 882 (2021).

59. K. Huda, C. Wu, J. G. Sider, and C. L. Bayer, "Spherical-view photoacoustic tomography for monitoring *in vivo* placental function," Photoacoustics **20**, 100209 (2020).

60. Y. Zhang and L. Wang, "Video-rate ring-array ultrasound and photoacoustic tomography," IEEE Trans. Med. Imaging. **39**, 4369 (2020).

61. H. Estrada, A. Ozbek, J. Robin, S. Shoham, and D. Razansky, "Spherical array system for high-precision transcranial ultrasound stimulation and opto-acoustic imaging in rodents," IEEE Trans. Ultrason. Ferroelectr. Freq. Control. **68**, 107 (2021).

62. M. Heijblom, W. Steenbergen, and S. Manohar, "Clinical photoacoustic breast imaging: the Twente experience," IEEE Pulse **6**, 42 (2015).

63. F. Zheng, X. Zhang, C. T. Chiu, B. L. Zhou, K. K. Shung, H. F. Zhang, and S. Jiao, "Laser-scanning photoacoustic microscopy with ultrasonic phased array transducer," Biomed. Opt. Express **3**, 2694 (2012).

64. S. Li, Q. Deng, Y. Zhang, X. Li, G. Wen, X. Cui, Y. Wan, Y. Huang, J. Chen, Z. Liu, L. Wang, and C. S. Lee, "Rational design of conjugated small molecules for superior photothermal theranostics in the NIR-II biowindow," Adv. Mater. **32**, 2001146 (2020).

65. G. Wen, X. Li, Y. Zhang, X. Han, X. Xu, C. Liu, K. W. Y. Chan, C. S. Lee, C. Yin, L. Bian, and L. Wang, "Effective phototheranostics of brain tumor assisted by near-infrared-II light-responsive semiconducting polymer nanoparticles," ACS Appl. Mater. Interfaces. **12**, 33492 (2020).

66. M. Zha, X. Lin, J. S. Ni, Y. Li, Y. Zhang, X. Zhang, L. Wang, and K. Li, "An ester-substituted semiconducting polymer with efficient nonradiative decay enhances NIR-II photoacoustic performance for monitoring of tumor growth," Angew. Chemie–Int. Ed. **59**, 23268 (2020).

67. J. Zhang, G. Wen, W. Wang, K. Cheng, Q. Guo, S. Tian, C. Liu, H. Hu, Y. Zhang, H. Zhang, L. Wang, and H. Sun, "Controllable cleavage of C–N bond-based fluorescent and photoacoustic dual-modal probes for the detection of H₂S in living mice," ACS Appl. Bio Mater. **4**, 2020 (2021).

68. J. Xia, C. Kim, and J. F. Lovell, "Opportunities for photoacoustic-guided drug delivery," Curr. Drug Targets. **16**, 571 (2015).

69. N. Gandhi, M. Allard, S. Kim, P. Kazanzides, and M. A. L. Bell, "Photoacoustic-based approach to surgical guidance performed with and without a da Vinci robot," J. Biomed. Opt. **22**, 121606 (2017).

70. Z. Wu, L. Li, Y. Yang, P. Hu, Y. Li, S. Y. Yang, L. V. Wang, and W. Gao, "A microrobotic system guided by photoacoustic computed tomography for targeted navigation in intestines *in vivo*," Sci. Robot **4**, eaax0613 (2019).

71. L. Labanieh, R. G. Majzner, and C. L. Mackall, "Programming CAR-T cells to kill cancer," Nat. Biomed. Eng. **2**, 377 (2018).

72. A. Aziz, M. Medina-Sánchez, J. Claussen, and O. G. Schmidt, "Real-time optoacoustic tracking of single moving micro-objects in deep phantom and *ex vivo* tissues," Nano Lett. **19**, 6612 (2019).

73. Y. Yan, W. Jing, and M. Mehrmohammadi, "Photoacoustic imaging to track magnetic-manipulated micro-robots in deep tissue," Sensors **20**, 2816 (2020).

74. G. S. Jeng, M. L. Li, M. W. Kim, S. J. Yoon, J. J. Pitre, D. S. Li, I. Pelivanov, and M. O'Donnell, "Real-time interleaved spectroscopic photoacoustic and ultrasound (PAUS) scanning with simultaneous fluence compensation and motion correction," Nat. Commun. **12**, 716 (2021).

75. H. Su, "Optical-resolution photoacoutic microscopy," PhD Dissertation (Washington University in St. Louis, 2010).

76. K. Maslov, H. F. Zhang, S. Hu, and L. V. Wang, "Optical-resolution photoacoustic microscopy for *in vivo* imaging of single capillaries," Opt. Lett. **33**, 929 (2008).

77. S. Hu, K. Maslov, and L. V. Wang, "Second-generation optical-resolution photoacoustic microscopy with improved sensitivity and speed," Opt. Lett. **36**, 1134 (2011).

78. Y. Liang, J.-W. Liu, L. Jin, B.-O. Guan, and L. Wang, "Fast-scanning photoacoustic microscopy with a side-looking fiber optic ultrasound sensor," Biomed. Opt. Express **9**, 5809 (2018).

79. B. Rao, K. Maslov, A. Danielli, R. Chen, K. K. Shung, Q. Zhou, and L. V. Wang, "Real-time four-dimensional optical-resolution photoacoustic microscopy with Au nanoparticle-assisted subdiffraction-limit resolution," Opt. Lett. **36**, 1137 (2011).

80. W. Qin, T. Jin, H. Guo, and L. Xi, "Large-field-of-view optical resolution photoacoustic microscopy," Opt. Express **26**, 4271 (2018).

81. C. Zhang, H. Zhao, S. Xu, N. Chen, K. Li, X. Jiang, L. Liu, Z. Liu, L. Wang, K. K. Y. Wong, J. Zou, C. Liu, and L. Song, "Multiscale high-speed photoacoustic microscopy based on free-space light transmission and a MEMS scanning mirror," Opt. Lett. **45**, 4312 (2020).

82. J. Lee, S. Han, D. Seong, J. Lee, S. Park, R. Eranga Wijesinghe, M. Jeon, and J. Kim, "Fully waterproof two-axis galvanometer scanner for enhanced wide-field optical-resolution photoacoustic microscopy," Opt. Lett. **45**, 865 (2020).

83. L. Wang, K. Maslov, and L. V. Wang, "Single-cell label-free photoacoustic flowoxigraphy *in vivo*," Proc. Natl. Acad. Sci. U. S. A. **110**, 5759 (2013).

84. L. Wang, K. Maslov, J. Yao, B. Rao, and L. V. Wang, "Fast voice-coil scanning optical-resolution photoacoustic microscopy," Opt. Lett. **36**, 139 (2011).

85. J. Chen, Y. Zhang, L. He, Y. Liang, and L. Wang, "Wide-field polygon-scanning photoacoustic microscopy of oxygen saturation at 1-MHz A-line rate," Photoacoustics. **20**, 100195 (2020).

86. J. Y. Kim, C. Lee, K. Park, S. Han, and C. Kim, "High-speed and high-SNR photoacoustic microscopy based on a galvanometer mirror in non-conducting liquid," Nat. Publ. Gr. **6**, 34803 (2016).

87. J. Y. Kim, C. Lee, K. Park, G. Lim, and C. Kim, "Fast optical-resolution photoacoustic microscopy using a 2-axis water-proofing MEMS scanner," Sci. Rep. **5**, 7932 (2015).

88. B. Lan, W. Liu, Y. Wang, J. Shi, Y. Li, S. Xu, H. Sheng, Q. Zhou, J. Zou, U. Hoffmann, W. Yang, and J. Yao, "High-speed widefield photoacoustic microscopy of small-animal hemodynamics," Biomed. Opt. Express **9**, 4689 (2018).